Anomalously porous boulders on (162173) Ryugu as primordial materials from its parent body

N. Sakatani [1✉], S. Tanaka [2,3,4], T. Okada [2,5], T. Fukuhara[1], L. Riu [2], S. Sugita [5], R. Honda[6], T. Morota [5], S. Kameda [1], Y. Yokota[2], E. Tatsumi [5,7], K. Yumoto [5], N. Hirata [8], A. Miura[2], T. Kouyama[9], H. Senshu[10], Y. Shimaki [2], T. Arai[11,36], J. Takita[12], H. Demura[8], T. Sekiguchi [13], T. G. Müller[14], A. Hagermann[15], J. Biele [16], M. Grott [17], M. Hamm [17,18], M. Delbo [19], W. Neumann [17,20], M. Taguchi[1], Y. Ogawa[8], T. Matsunaga[21], T. Wada[2], S. Hasegawa[2], J. Helbert [17], N. Hirata[22], R. Noguchi[2], M. Yamada[10], H. Suzuki[23], C. Honda[8], K. Ogawa [24], M. Hayakawa[2], K. Yoshioka[4], M. Matsuoka [2], Y. Cho[5], H. Sawada[2], K. Kitazato[8], T. Iwata [2,3], M. Abe[2], M. Ohtake[8], S. Matsuura [25], K. Matsumoto[3,26], H. Noda[3,26], Y. Ishihara[24], K. Yamamoto[26], A. Higuchi [27], N. Namiki [3,26], G. Ono[28], T. Saiki[2], H. Imamura [2], Y. Takagi[29], H. Yano [2,3], K. Shirai[22], C. Okamoto[22,37], S. Nakazawa [2], Y. Iijima[2,37], M. Arakawa [22], K. Wada[10], T. Kadono [27], K. Ishibashi[10], F. Terui[2], S. Kikuchi[2], T. Yamaguchi[30], N. Ogawa[2], Y. Mimasu[2], K. Yoshikawa[2], T. Takahashi[31], Y. Takei [2], A. Fujii [2], H. Takeuchi [2,3], Y. Yamamoto [2], C. Hirose[2], S. Hosoda [2], O. Mori [2], T. Shimada[2], S. Soldini [32], R. Tsukizaki [2], M. Ozaki [2,3], S. Tachibana [5], H. Ikeda[2], M. Ishiguro[33], H. Yabuta[34], M. Yoshikawa[2,3], S. Watanabe [35] and Y. Tsuda[2,3]

Planetesimals—the initial stage of the planetary formation process—are considered to be initially very porous aggregates of dusts[1,2], and subsequent thermal and compaction processes reduce their porosity[3]. The Hayabusa2 spacecraft found that boulders on the surface of asteroid (162173) Ryugu have an average porosity of 30–50% (refs. [4–6]), higher than meteorites but lower than cometary nuclei[7], which are considered to be remnants of the original planetesimals[8]. Here, using high-resolution thermal and optical imaging of Ryugu's surface, we discovered, on the floor of fresh small craters (<20 m in diameter), boulders with reflectance (~0.015) lower than the Ryugu average[6] and porosity >70%, which is as high as in cometary bodies. The artificial crater formed by Hayabusa2's impact experiment[9] is similar to these craters in size but does not have such high-porosity boulders. Thus, we argue that the observed high porosity is intrinsic and not created by subsequent impact comminution and/or cracking. We propose that these boulders are the least processed material on Ryugu and represent remnants of porous planetesimals that did not undergo a high degree of heating and compaction[3]. Our multi-instrumental analysis suggests that fragments of the highly porous boulders are mixed within the surface regolith globally, implying that they might be captured within collected samples by touch-down operations[10,11].

Hayabusa2 carried out descending operations[10], where the thermal infrared camera (TIR) acquired high-resolution images below 500 m altitude, resulting in spatial resolutions better than 45 cm per pixel (Extended Data Fig. 1). To find the low-thermal-inertia (TI) and high-porosity area, which should show higher daytime temperature, we investigated the average temperatures and their standard deviations for each descent sequence (Supplementary Table 1) and searched for regions where the brightness temperature differed by more than two standard deviations from the average. As expected, the hot regions are generally located at
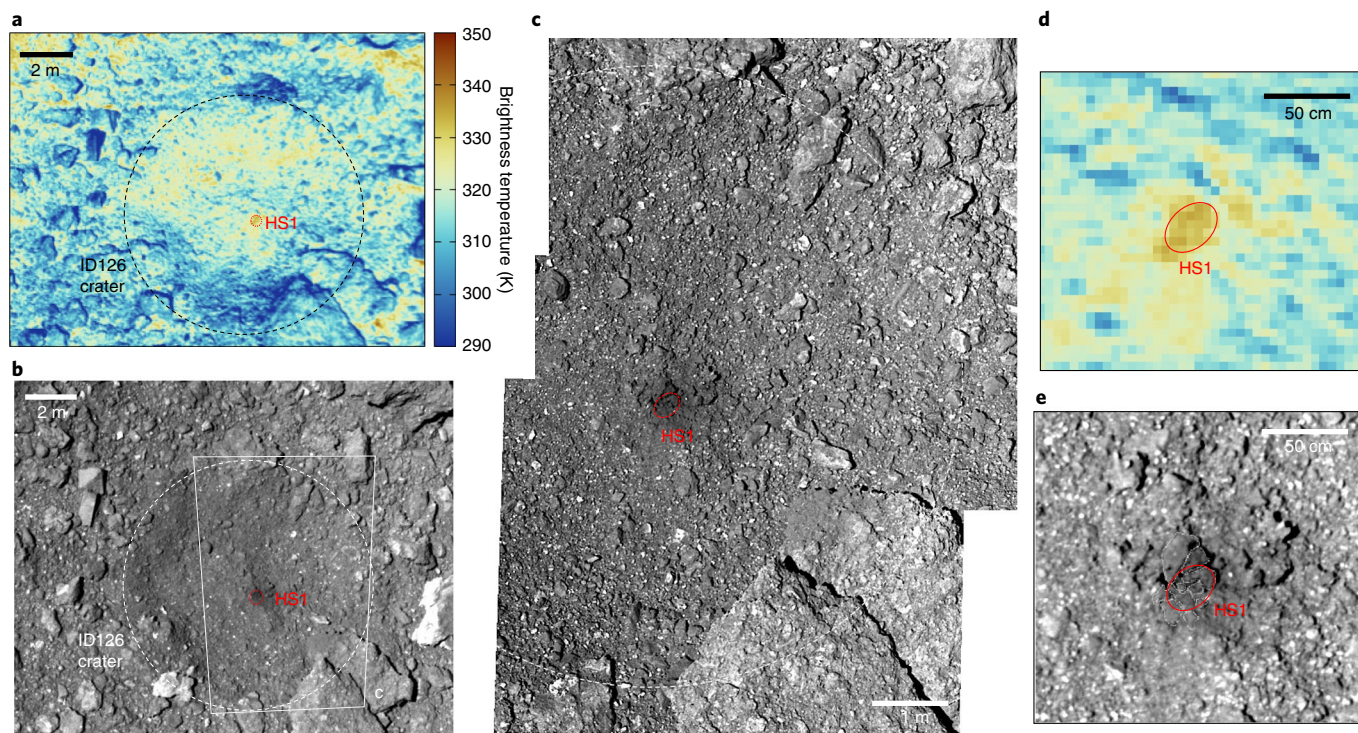
Fig. 1 | Hotspot HS1 within the ID126 crater. a, TIR image of the ID126 crater (hyb2_tir_20181015_133900_l2). The black dashed and red solid circles show the crater rim and hotspot HS1. **b**, ONC-T image of the ID126 crater (hyb2_onc_20181025_025356_twf_l2b). **c**, Mosaic image created from two ONC-T images acquired during TD1-R1A (hyb2_onc_20181015_133833_tvf_l2b) and TD1-R3 (hyb2_onc_20181025_022806_tvf_l2b). **d**, Close-up TIR image (hyb2_tir_20181025_022832_l2) of HS1. **e**, Close-up ONC-T image (hyb2_onc_20181025_022806_tvf_l2b). The hotspot corresponds to the region enclosed by the red ellipse, which consists of 10-cm-sized boulders, whose outlines are indicated by white lines. See also Fig. 3e for a composite of the TIR and ONC-T images.

solar-directed boundaries between the boulders and the ground, where self-heating by solar reflection and radiation from the boulder's side wall is strong. Moreover, two isolated hotspots were found (Extended Data Fig. 2).

The most definitive hotspot is a high-temperature boulder assembly (HS1, Fig. 1) located near the centre of a small crater with a diameter of approximately 9 m, catalogued as the ID126 crater located at 4.8° N, 212.4° E (ref.[12]). The size of HS1 is about 40 cm and it consists of a few boulders of tens of centimetres in size based on multiband optical navigation camera telescope (ONC-T) images, which might imply breakup of a parent boulder during the cratering process. On the basis the image shown in Fig. 1d, the temperature of HS1 corresponds to an apparent TI of 73 ± 25 J m^{-2} K^{-1} s$^{-0.5}$, hereafter 'tiu' (see Methods and Extended Data Fig. 3), notably lower than Ryugu's global average of 200–400 tiu (refs. [5,13]). One might attribute the low TI to fine-grained dust deposits[14,15]. Although the presence of dusts with particle sizes of a few hundred micrometres on Ryugu's surface and/or subsurface is indicated by camera images taken during the touch-down operations[11], no such dust layer was found on boulders according to in situ observations by the Mobile Asteroid Surface Scout (MASCOT) lander[4,16]. Furthermore, the HS1 boulders show clear outlines and a brightness contrast on the surface (Fig. 1e), thus a thick dust deposit is unlikely. The observed low TI should therefore stem from the intrinsic insulating and thus porous nature of the boulders. Although a surface dust coating thinner than the camera resolution cannot be ruled out based on the TIR daytime data, it is unlikely to play a major role based on local observations at the MASCOT landing site[4,15]. According to the empirical relations between thermal conductivity and porosity (Methods), the corresponding porosity ϕ is taken as 72–91%.

Furthermore, we found another hotspot (HS2) with potentially low TI comparable with HS1 (Fig. 2). HS2 (~3 m in diameter) is also located at the centre of the crater catalogued as ID69 located at 9.6° N, 149.1° E, whose rim-to-rim diameter is 20 m (ref. [17]). The apparent TI of HS2 is 53 ± 49 tiu. Unfortunately, high-resolution ONC-T images of this crater could not be acquired; thus its detailed morphology is difficult to examine. The question of whether HS2 consists of boulders like HS1 or fine-grained regolith ponds like those found in craters on Eros[18] therefore remains unknown. Under the assumption that HS2 consists of boulders, we estimate $\phi > 71\%$.

Out of seven catalogued craters[17] whose centres are pictured by the TIR images (Extended Data Fig. 1), only the two smallest ones (ID126 and ID69) have central hotspots. For example, crater ID46 does not show any hotspot signature (Extended Data Fig. 4a). Furthermore, global observations from 5 km altitude showed no detectable hotspots in large (and old) craters (Supplementary Fig. 1). An artificial impact crater formed by the small carry-on impactor (SCI) experiment[9] provides useful information for understanding the thermophysical properties of fresh craters. The highest-resolution TIR image (23 cm per pixel) showed no detectable hotspot in the SCI crater (Extended Data Fig. 5a,b). Thermal simulations using a local digital elevation model[9] showed that the observed temperatures are consistent with the simulated temperature if a uniform TI of 300 tiu, comparable to the global average, is assumed (Extended Data Fig. 5c,d). We therefore suggest that low-TI material like HS1 and HS2 is not buried in the subsurface of this region or that this material is exposed in patches smaller than the pixel resolution in small quantities relative to more thermophysically common boulders. The absence of a hotspot in the SCI crater also indicates that the low-TI and high-porosity nature of the
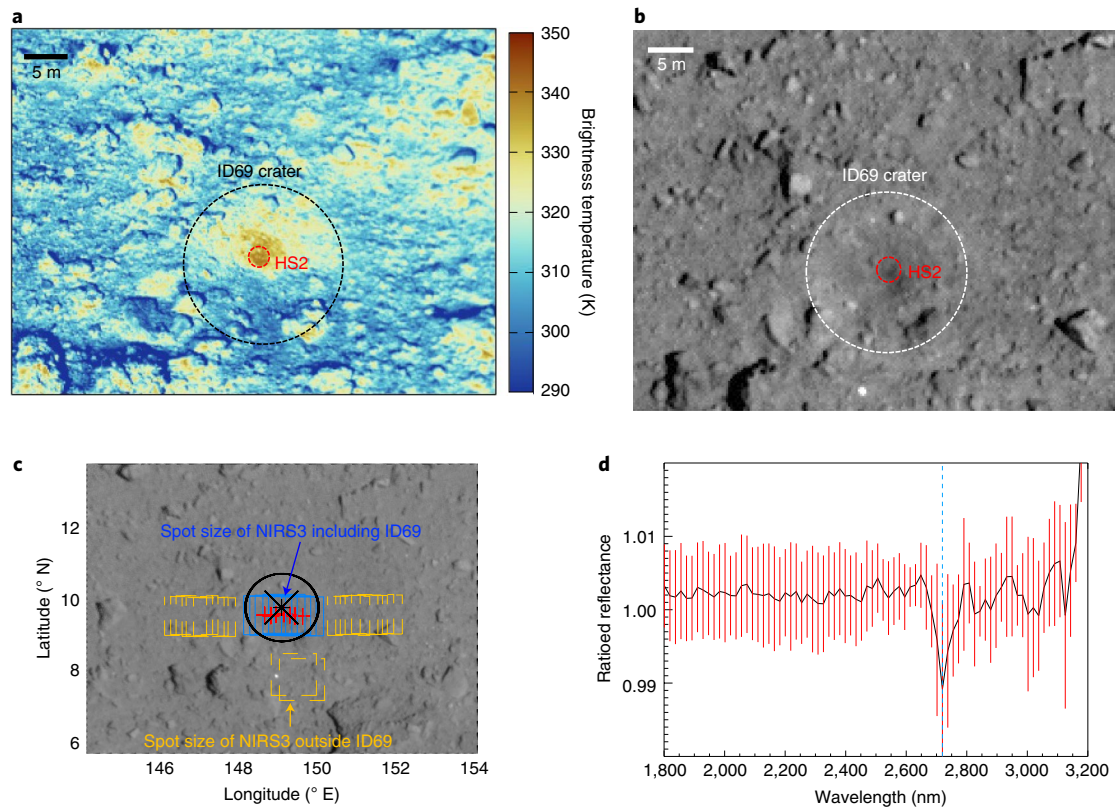
Fig. 2 | Hotspot HS2 observed by TIR and NIRS3 observation. a, TIR image of the ID69 crater (9.6° N, 149.1° E) with hotspot HS2 (hyb2_tir_20180921_034132_l2). **b**, ONC-T image of the ID69 crater (hyb2_onc_20190221_154026_tvf_l2b). This image was acquired after the solar conjunction in December 2019, whereas the TIR image in **a** was collected previously, thus the shadow direction is different in each image. **c**, NIRS3 footprint around the ID69 crater on 31 October 2018. The black circle represents the rim of the crater, and its centre is denoted by the black cross. The blue and yellow rectangles denote the NIRS3 spot sizes inside and outside the crater, respectively. The red crosses indicate the centres of NIRS3 observation footprints inside the crater. **d**, NIRS3 spectra of the crater including HS2 normalized to the spectra outside of the ID69 crater. A relatively stronger 2.72 μm absorption feature marked with the vertical blue dashed line is found in the crater. Error bars are calculated from equation (8) in the Methods.

hotspots is unlikely to be due to single impact comminution and shock-induced cracks.

We investigated the brightness temperatures of boulders identified in six sets of the TIR and ONC-T images during the touch-down rehearsal (TD1-R3) sequence[10] (Fig. 3a–f and Extended Data Fig. 6). HS1's temperature exceeds that of all other boulders by 10 K (Fig. 4a), which strongly suggests that it has the lowest TI. Approximately 70% of the boulders have TI consistent with the global average of 200–400 tiu (Extended Data Fig. 7b). In addition to the anomalously low TI, HS1 is the darkest among the boulders and regolith. We found a positive correlation between TI and v-band (0.55 μm in wavelength) reflectance (Fig. 4c). Asteroid (101955) Bennu shows a similar correlation[19], and this trend in common in both carbonaceous asteroids may originate from some universal physical/chemical processes in their parent bodies. The trend is discontinuous and three groups appear: the hotspots (HS1 and HS2) with low reflectance, a cluster with intermediate reflectance and TI consistent with Ryugu's global average[5,6,13], and the bright boulders with high TI (so-called bright/cold spots[5,20]). Visible spectral slopes from 0.55 to 0.86 μm for HS1 and HS2 are contrastive; the former is redder than the clustered boulders and the latter is bluer but consistent with the common boulders (Fig. 4b,d). It could be argued that the anomalous properties of the HS1 have an exogenous origin, for instance, from the infall of porous and dark comet-like materials. However, this hypothesis is not likely because on the TI–reflectance, TI–colour and reflectance–colour diagrams, the regolith lies on a mixing line

between the common boulders and HS1. Because of this, we favour the hypothesis that the HS1 material is an original constituent of asteroid Ryugu and small HS1-like boulder fragments are mixed into the regolith. Note that the mixing model in the TI will be effective if the fragmented regolith grains are comparable in size to or larger than the thermal skin depth of the porous materials (~1 cm); for smaller grain sizes, the TI of the mixed fragments is dominated by the grain size themselves, and microporosity is less relevant[21].

Global observations by the near-infrared spectrometer NIRS3 revealed weak absorption features of the hydroxyl-related band at 2.72 μm, similar to spectral features of heated and partially dehydrated carbonaceous chondrites[22]. The primary partial dehydration is thought to be caused by radiogenic heating following the formation of hydrous silicates in the parent body, and solar radiative heating of Ryugu's top-surface materials when Ryugu was nearer to the Sun in the past resulted in the additional dehydration[23]. Although there are no NIRS3 data to resolve crater ID126, the ID69 crater data indicate a 2.72 μm absorption band slightly deeper than the surroundings (Fig. 2c,d), whereas the ID46 crater without the hotspot does not show such an increase in the absorption feature (Extended Data Fig. 4c,d). This supports that the ID69 crater including the low-TI materials is fresher and would experience less radiative heating on the surface. On the other hand, the band depth also depends on the porosity itself[24]. The alternative interpretation of the NIRS3 data is that the high-porosity nature of HS2 materials in crater ID69 might make the absorption deeper.
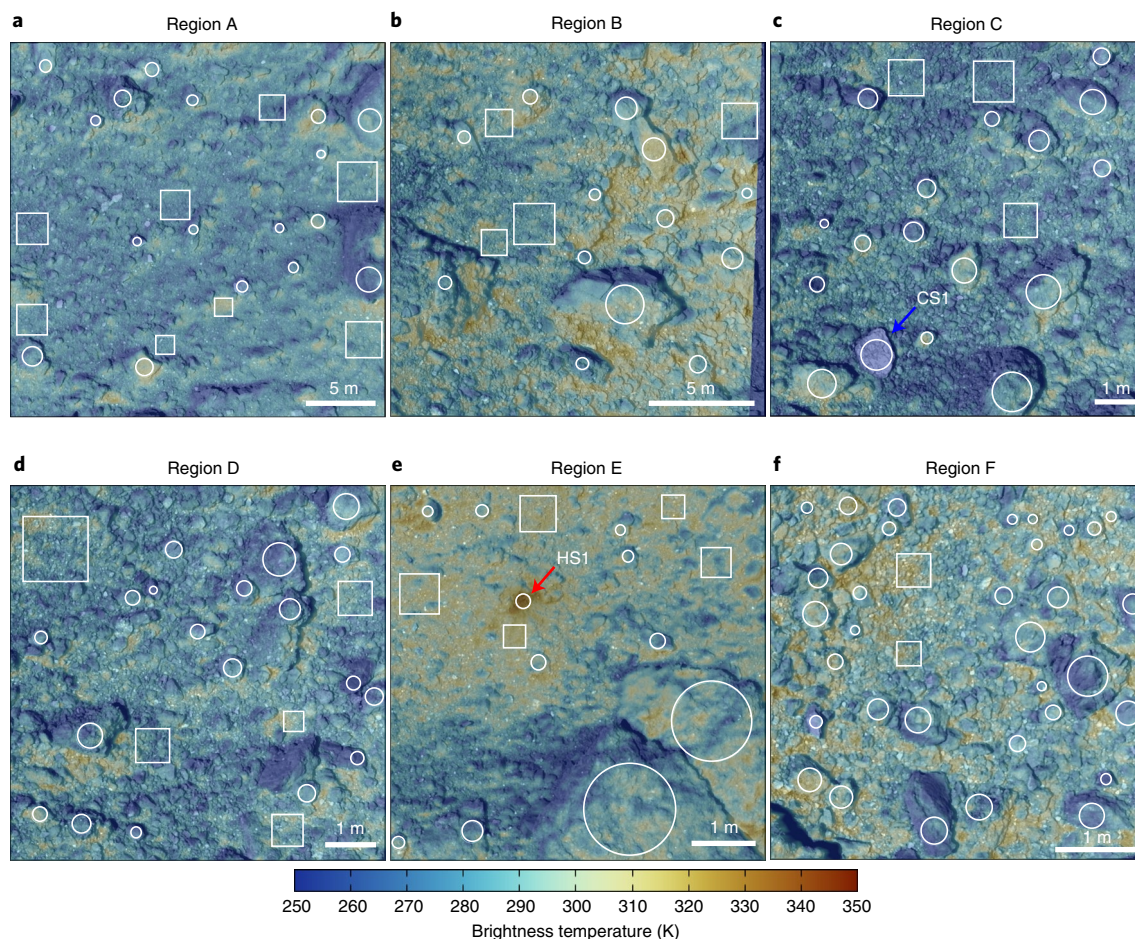
Fig. 3 | TIR temperature images overlain on the ONC-T images acquired during the TD1-R3 sequence. a–f, We examined these six regions (regions A to F) where ONC-T images covered the field of view of TIR images in this descent sequence. Centre latitude and longitude of these images based on LIDAR-derived trajectory are 4.5° N, 235.9° E for region A (**a**), 4.5° N, 224.8° E for region B (**b**), 4.8° N, 215.5° E for region C (**c**), 4.9° N, 213.8° E for region D (**d**), 4.9° N, 212.2° E for region E (**e**) and 4.8° N, 210.5° E for region F (**f**) (see also Extended Data Fig. 1d). White circles and squares indicate regions where the temperature, v-band (550 μm in wavelength) reflectance factor at standard geometric conditions ([i, e, α] = [30°, 0°, 30°], where i, e and α are incident, emission and solar phase angles, respectively), and v-band to x-band (860 μm) slope were measured for the boulders and regolith (region mainly with grains unresolved from images with resolutions of 26 to 4.4 mm per pixel), respectively, as shown in Fig. 4. The red arrow indicates hotspot HS1, and the blue arrow indicates cold and bright spot CS1[5,20]. Hotspot HS2 is located outside the displayed regions. Images of HS2 can be seen in Extended Data Fig. 6g, acquired during the descent operations for deployment of Micro Nano Experimental Robot Vehicle for Asteroid, the Second Generation (MINERVA-II).

Porosity of the hotspot boulders ($\phi > 70\%$) is as high as bulk porosity of comets and trans-Neptunian objects[25], which are thought to preserve the primordial accretion process of dusts or pebbles in the outer protoplanetary disk[8]. We state that the most likely origin of HS1-like materials is the dust aggregation process during the formation of the planetesimal of Ryugu's parent body, in which the highly porous materials are theoretically and experimentally predicted[2,26] (see Methods for other potential processes enhancing the porosity). Furthermore, because our study detected hotspots only in the centres of small fresh craters, we suggest that the porous boulders survived in the subsurface and were excavated by impacts (Fig. 5e,f). Once exposed at the surface, they were selectively disrupted into small fragments by surface activities, such as micrometeoroid impacts and/or thermal fatigue[27], because of their comparatively lower mechanical strength (Fig. 5c). Concentrations of these fragmented fine grains, which is expected to result in lower TI than hotspot boulders[21], are not observed by TIR; relatively rapid transportation can therefore be expected to occur on Ryugu's surface (Fig. 5d). One of the most likely processes of the fragment transportation is dust levitation by electric potential differences[28].

The inherent origin of the highly porous materials indicates that they were derived from the uppermost part of a partially consolidated layer on a planetesimal, and are likely to be the most primitive among Ryugu's boulders without a high degree of thermal alteration and compaction in the parent body (Fig. 5a). Indeed, a model of the planetesimal compaction[29] suggests that such highly porous and partially consolidated materials have experienced temperatures lower than 600 K at the near surface, whereas the more compact materials were exposed to a hotter interior (see Methods and Extended Data Fig. 8). In Hayabusa2's first touch-down and sampling operation, dark and red dust particles consistent with HS1 optical properties were excavated from the surface by the thruster jet[11]. These dust grains have been interpreted as materials that experienced solar radiative heating[11]. Our analysis presents an alternative hypothesis that the excavated dark/red dusts are the fragments of HS1-like boulders, as remnants of less-processed planetesimals. Laboratory analysis of the collected samples, in which these primitive materials could be included, will help to reveal the nature of planetesimals as a starting point of the planetary formation process.
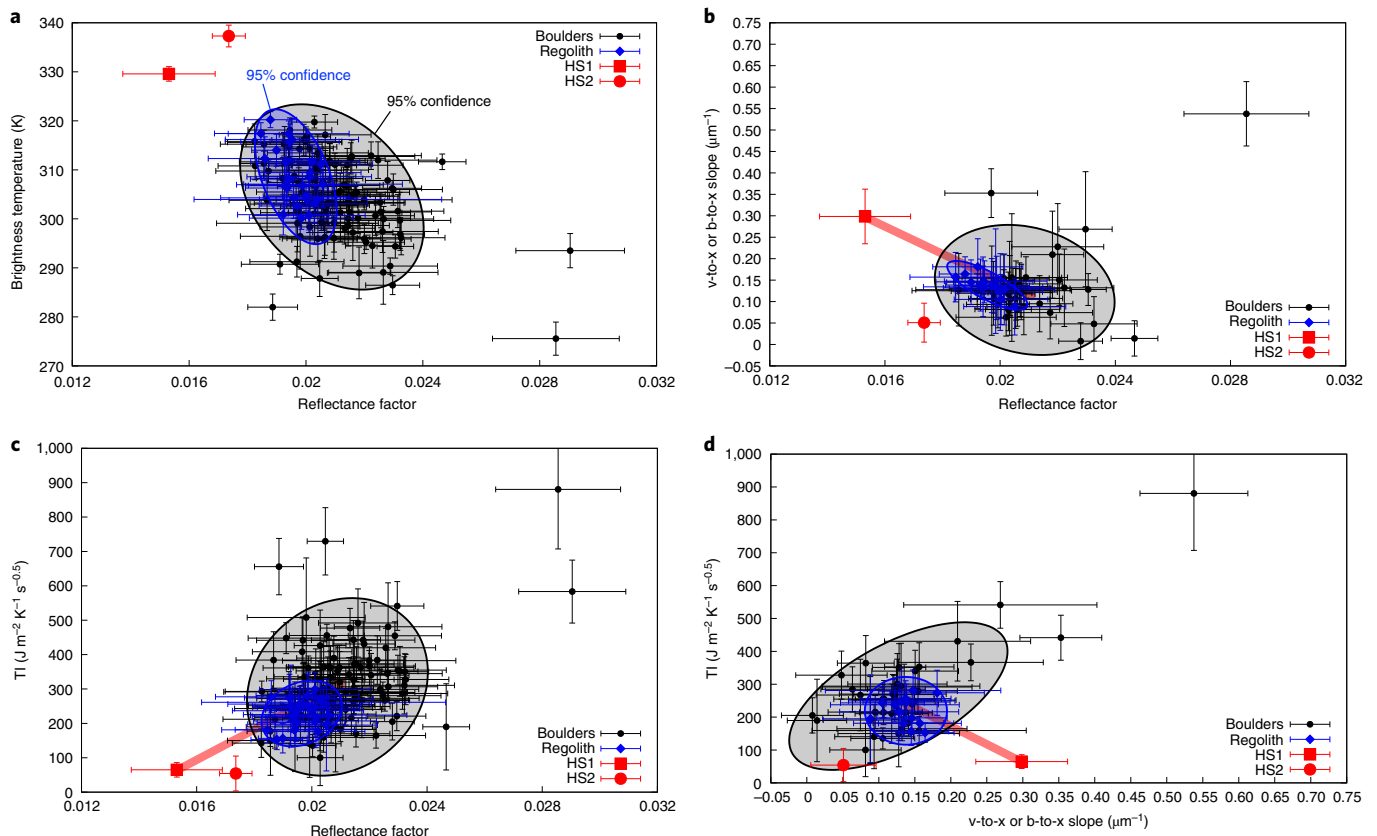
Fig. 4 | Thermal and optical properties of boulders and regolith on Ryugu. a–d, Correlation between temperature and v-band reflectance (**a**), v-to-x slope and reflectance (**b**), TI and reflectance (**c**) and TI and v-to-x slope (**d**). Black and blue points represent boulders and regolith, respectively. Error bars for each point represent the standard deviation in the counted area. The red square represents hotspot HS1 and the red circle represents hotspot HS2. Because the multiband imaging sequence is spatially discrete, the number of boulders with spectral information is limited. Grey (boulders) and blue (regolith) clouds show 95% (2σ) probability regions assuming two-dimensional Gaussian distributions, except for the two brightest boulders. Red lines in **b–d**, connecting the HS1 and centre of the boulder distribution, indicate mixing lines between HS1 and abundant boulders, along which the regolith-rich regions are mapped. These mixing lines imply that fragments from the HS1-like materials are included in the regolith.

Methods

Thermal simulation and TI estimate. We have developed a thermal simulation code using a given shape model that can output the one-rotation temperature history for all facets at arbitrary spin parameters and asteroid position in equatorial coordinates relative to the Sun[5,13,30]. This model solves the one-dimensional heat conduction equation for each facet of the shape model, including the effect of solar isolation from the surrounding topography, input of thermal radiation and solar reflection from the other facets (so-called self-heating). The albedo is uniformly set to 0.0146 (bond albedo[31]) and the emissivity is 1.0 for compatibility with the brightness temperature (equivalent blackbody temperature) data. The spin parameters are based on the public version of SPICE PCK kernel (hyb2_ryugu_shape_v20190328.tpc, https://www.darts.isas.jaxa.jp/pub/hayabusa2/spice_bundle/spice_kernels/), the rotational period is 7.6326 h, and the ecliptic longitude and latitude of the spin axis are 179.091° and −87.428°, respectively.

We performed simulations using two different shape models. One is a global shape model, named SHAPE_SPC_3M_v20190328 based on stereo-photoclinometry[17], to derive the apparent TI of the boulders and regolith in regions A to F (Fig. 3). For efficiency, we cut out regional data (rectangular regions in longitude–latitude coordinates) including the region of interest from the global model. The facet size of the global shape model is roughly 1 m, which is larger than the pixel resolution of the TIR image in the descent sequence described in this paper (<45 cm). The other shape model is the local digital elevation model around the SCI crater constructed using high-resolution ONC-T images[9]. The facet size used for the thermal simulation is approximately 20 cm, which is comparable with the spatial resolution of the TIR image in Extended Data Fig. 5.

TI is typically estimated from diurnal temperature profiles[32]. Nighttime cooling curves are especially sensitive to the TI and layered structure of the top surface[15]. Because the number of high-resolution images and range of local-time observations for a single target region is limited, we could not examine the entire diurnal temperature history of the boulders and regolith. TI must be estimated by comparing the observed temperature with simulated temperatures at given

times. We created simulated images by rendering of the three-dimensional temperature data[33] with TI ranging from 20 to 1,000 J m⁻² K⁻¹ s⁻⁰·⁵ (hereafter, 'tiu'). The spacecraft position relative to Ryugu's fixed frame at the observation epoch was derived from improved trajectory data using the post-evaluated trajectory after the operation and altitude information of the laser altimeter (LIDAR)[34]. From the simulated temperature images, we averaged the pixel values within latitude and longitude ranges for each region and then compared these with the observed temperatures of the respective boulders and regolith. The apparent TI, Γ, was determined by linear interpolation of the calculated temperature as:

$$\Gamma = \frac{\Gamma_{i+1} - \Gamma_i}{T_{i+1} - T_i}(T_{obs} - T_i) + \Gamma_i \qquad (1)$$

where Γ_i is the TI chosen in the ith simulation ($\Gamma_i = 20, 50, 100, 200$ tiu … for $i = 0, 1, 2, 3, …$), T_i is the simulated temperature when Γ_i is assumed, and T_{obs} is the mean observed temperature of the boulders or regolith ($T_i < T_{obs} < T_{i+1}$). Using the standard deviations of T_i and T_{obs} within the averaged regions, the uncertainty of the estimated TI is calculated according to the error propagation via above the equation. Extended Data Fig. 3a,b shows how to determine the apparent TI of HS1, yielding TI = 73 ± 25 tiu. The ID69 crater is topographically resolved in the global shape model. The simulated temperatures were then averaged within the hotspot region and compared with the observed temperature of HS2 (Extended Data Fig. 3c,d). The apparent TI of HS2 is 53 ± 49 tiu. The larger error of HS2 can be attributed to the heterogeneous temperature distributions in both the observations and the simulation. Extended Data Fig. 7b shows a histogram of the TI for the boulders in regions A–F (Figs. 3 and 4) and the HS2 hotspot.

Possible uncertainties in TI. During the touch-down rehearsal (TD1-R3) sequence on 25 October 2018, the local solar incident angle of the observed region was lower than that in the other sequences (Supplementary Table 1). It is reasonable to focus on the TD1-R3 data to minimize the disturbance of the
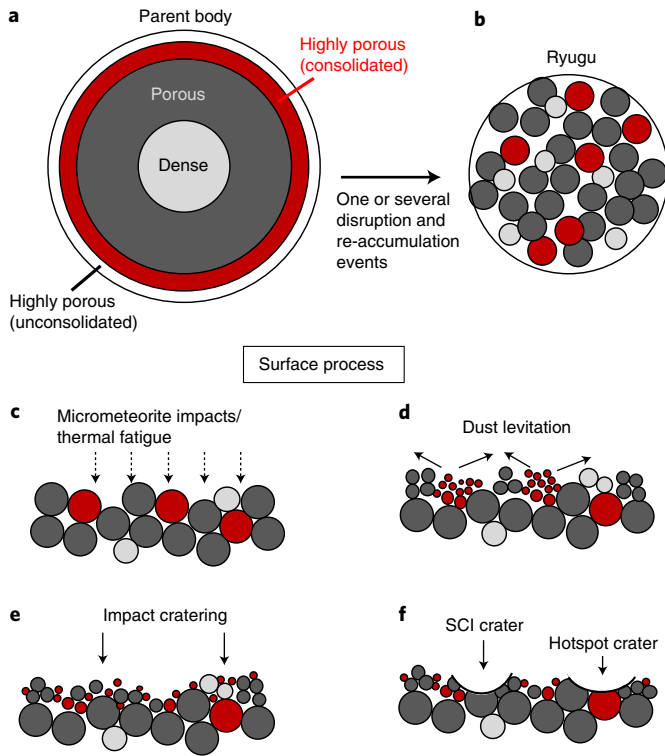
Fig. 5 | Formation process and surface behaviour of the hotspot boulders.
a, Layered or gradual porosity forms in the parent body owing to the thermal evolution and compaction process (Methods and Extended Data Fig. 8). **b**, Its catastrophic disruption and subsequent accumulation of the fragments form a precursor of Ryugu. **c**, On the asteroid surface, highly porous hotspot materials are selectively fragmented by micrometeorite impacts and/or thermal fatigue owing to weak mechanical strength. **d**, The fragmented grains are transported horizontally and mixed into the regolith and/or released into space by dust levitation. **e**, Crater formations occur on the surface. **f**, Surviving porous boulders in the subsurface are exposed. The absence of a hotspot in the SCI crater indicates a heterogeneous distribution of the large and porous boulders in the subsurface.

apparent temperature caused by the roughness effect, which is effective at higher solar phase angle[13], and by the uncertainty of the local slope of the boulder's surface, which is not reproduced in the global shape model.

Figure 4a indicates a negative correlation between temperature and reflectance. Brighter materials generally have lower temperatures owing to less absorption of the solar energy. However, because the reflectance factor ranges from 0.015 to 0.029 and the radiative equilibrium temperature is related to 1/4th power of the absorption coefficient given by 1 minus reflectance, the relative difference of the reflectance affects the temperature by only 0.4%. In a similar way, although dark materials might have higher infrared emissivity, emissivity does not substantially contribute the temperature difference. The variation of brightness temperature shown in Fig. 4a is therefore less affected by the reflectance and emissivity, and rather is due to true differences in TI.

Additional TI uncertainties arise from the local topography, which are not represented in the global shape model. The first is the local slope relative to the Sun, the second is crater topography and the third is the surface roughness; all of them affect the simulated apparent temperature. In the case of maximum solar illumination, the highest temperature of HS1 might be explained even by the higher TI. For example, the average solar incident angle $i = 24°$ is derived from the global shape model for region E, including HS1, at the observation epoch (25 October 2018, 02:28:32 UT). The radiative equilibrium temperature T_{eq}, or temperature with $\Gamma = 0$ tiu, is given by:

$$\epsilon \sigma T_{eq}^4 = (1 - A) S \left(\frac{R}{1\,\text{au}} \right)^{-2} \cos i, \qquad (2)$$

where ϵ is the emissivity, σ is the Stefan–Boltzmann constant, A is the albedo, S is the solar constant and R is the distance of Ryugu from the Sun. If this region, or HS1 boulders, directly faced the Sun ($i = 0°$), $T_{eq} = 357$ K is estimated, whereas

$T_{eq} = 349$ K for $i = 24°$. The effect of the solar illumination angle is therefore 8 K at a maximum and decreases when $\Gamma > 0$ tiu. The offset of 8 K in the simulation leads to higher TI of 130 tiu for the HS1 boulders, although this is an overestimate.

Furthermore, crater ID126 is not resolved in the global shape model and its detailed topography including the crater depth is unknown, so that the self-heating by the crater topography acts as an error source. To evaluate this effect, we performed thermal calculation without the self-heating using the local digital elevation model (DEM) of the SCI crater (Supplementary Fig. 2a). A differential image between the simulations with and without the self-heating shows that there are some regions with a very strong self-heating effect up to by 50 K. However, they correspond to the bases of boulders or low-temperature regions where direct solar energy input is relatively low. On the floor of the crater, the temperature enhancement by the self-heating is about 10–15 K, but local enhancement of the central temperature does not appear. If the hotspots were due to the self-heating effect and had similar TI to others in the craters, we expect that other boulders (and regolith) would have temperatures as high as the hotspots. But this is not the case from the TIR observations. Therefore, the hotspots should have lower TI than surrounding materials in the craters. We should also note that the SCI crater has a depth-to-diameter ratio of about 0.15 (ref. [9]), which is higher than small (<20 m) natural craters on Ryugu (<0.09)[17]. The self-heating is more effective for craters with a higher depth-to-diameter ratio, so the effect of the self-heating of the natural craters including ID69 and ID126 is lower than that of the SCI crater. In fact, the similar evaluation of the self-heating for ID69 craters (Supplementary Fig. 2b) showed that the self-heating contribution is about 5 K, which is less than observed temperature enhancement for the HS1 and HS2 hotspots (10 K and 20 K, respectively). Therefore, it is difficult to reproduce the hotspots by the self-heating effect of the crater topography.

Surface roughness, the typical scale of which is smaller than the facet sizes and TIR pixel resolution, reduces the apparent temperature of low-latitude regions[13]. The flat diurnal temperature profiles of Ryugu's surface[5] can be explained by a randomly rough surface model[35], which produces a lower temperature around noon and higher temperatures around dawn and dusk than the flat surface model[13]. Small shadows can be seen in the highest-resolution ONC image of HS1 (Fig. 1f), which reduce the apparent temperature. Thus, in contrast to the solar illumination condition and crater-related self-heating effect discussed above, TI values estimated using the model that does not account for roughness are upper limits. Similarly, high TI values are expected when using images with high solar phase angles and high emission angles. In fact, images in the TD1-R1A and TD1-L08E1 sequences yield higher TI for HS1 than TD1-R3. Nevertheless, the apparent TIs are less than 136 tiu (Supplementary Information and Supplementary Fig. 3). Because the temperatures of the hotspots are effectively higher than the other randomly selected boulders with various solar incident angles and HS1 and HS2 are seen as hotspots in all of the TIR data obtained with different solar illumination and viewing geometries (Extended Data Fig. 2), the TI of HS1 and HS2 is expected to be lower than that of the other boulders.

Porosity from TI. The TI Γ is related to thermal conductivity and porosity according to:

$$\Gamma = \sqrt{k \rho_s (1 - \phi) c}, \qquad (3)$$

where k is thermal conductivity, ϕ is boulder porosity, ρ_s is the material grain density and c is specific heat. Two empirical models were proposed for the relationship between k and ϕ on Ryugu based on the k data for chondritic meteorites[4]. Recent experimental studies using analogous porous rocks[36,37] and analytical studies of Ryugu's macroporosity[38] prefer the empirical model described as[4,39]:

$$k = 0.11 \frac{1 - \phi}{\phi} \qquad (4)$$

(solid curve in Extended Data Fig. 7a). With a grain density[38] of $\rho_s = 2,751\,\text{kg m}^{-3}$ and specific heat[40] as a function of the observed temperature T

$$c(T) = -23.173 + 2.127T + 1.5009 \times 10^2 T^2 - 7.3699 \times 10^{-5} T^3$$
$$+ 9.6552 \times 10^{-8} T^4, \qquad (5)$$

we calculated ϕ from the TI data. The resulting porosities are $86.3^{+4.3}_{-4.2}$% and $90.0^{+9.2}_{-8.4}$% for hotspots HS1 ($\Gamma = 73 \pm 25$ tiu) and HS2 ($\Gamma = 53 \pm 49$ tiu), respectively.

However, we note that the porosities of the measured meteorites and analogues are less than 50%, thus the estimated porosities are extrapolated values. Alternatively, micrometre-sized SiO_2 grain aggregates[41] cover a higher porosity range (40–90%). An preferred empirical relation between thermal conductivity and porosity is given as[42]:

$$k = 3.3[\exp(-50\phi) + \exp(-4.4 - 23.5\phi)]^{1/4} \qquad (6)$$

(dashed curve in Extended Data Fig. 7a). Applying this equation to the thermal conductivity, we derived porosities of $78.3^{+7.2}_{-5.9}$% and $84.2^{+15.6}_{-12.5}$% for

HS1 and HS2, respectively. Compression tests on the aggregates[43] showed that the highest-porosity aggregate ($\phi = 85\%$) is mechanically stable with a uniaxial compressional strength of approximately 500 Pa. Such fluffy aggregates might be also possible candidates of the hotspot materials on Ryugu as a remnant of the less-processed near-surface layer of planetesimals. We note that the thermal conductivity of dust aggregates[41] will be lower than that of rocks with the same porosity, because of the higher cohesion of the consolidated rock, with the grains probably held together by some sort of cement or sintered neck rather than just electrostatic forces alone. The enhanced grain-to-grain heat exchange hence increases thermal conductivity in consolidated rocks. Therefore, the porosities from this empirical equation may be underestimated. To derive an accurate porosity–conductivity relationship for the highly porous consolidated materials, measurements of thermophysical properties for the extremely porous and consolidated materials will be required by experimental studies.

Extended Data Fig. 7c shows a histogram of the boulder porosity based on this equation, which indicates that boulders with a porosity between 30% and 60% are dominant and small fractions of higher- and lower-porosity materials exist on Ryugu.

ONC-T spectral analysis. ONC-T multiband imaging was conducted during the descent operations from an altitude of approximately 500 m, according to the pre-registered timeline sequence. The acquired digital images were calibrated into radiance factors[44]. A photometric correction using the Ryugu photometric model[45] yielded the reflectance factor in the standard geometric condition with solar incident, emission and phase angles of 30°, 0° and 30°, respectively (left panels in Extended Data Fig. 6). We used the stereo-photoclinometry-based shape model and LIDAR-derived trajectory, as in the case for the TIR data analysis. Note that the shape model resolution is substantially lower than the image resolution. We selected the boulder with the facet towards cameras to avoid errors introduced by the photometric correction. The spectral slope from the v-band (0.55 μm in wavelength) to x-band (0.86 μm) is defined as:

$$S_{vx} = \frac{1 - R_x/R_v}{\lambda_v - \lambda_x}, \tag{7}$$

where R_v and R_x are the reflectance factors and λ_v and λ_x are the effective wavelengths for the v-band and x-band, respectively. Owing to the delay induced by rotating the filter wheel in the multiband images, the field of view of ONC-T slightly drifts, which results in a small overlap between different band images. The regions with spectral information are thus limited, and the spectral information of some boulders and regolith cannot be measured (right panels in Extended Data Fig. 6).

We used multiband images acquired during the descent sequence in TD1-R3 for regions A and B, whereas no high-resolution multiband data with boulder resolution were available for regions D and F. An image set of region C was obtained during the TD1-L08E1 operation on 21 February 2019 (Extended Data Fig. 6c). Multiband images were acquired for region E, including the ID126 crater, during the ascent phase of TD1-R3 at an altitude of approximately 230 m (Extended Data Fig. 6e). Unfortunately, the v-band image did not cover the ID126 crater; thus, b-band (0.48 μm) and x-band images were used for the spectral analysis of region E and b-to-x slope is used rather than v-to-x slope. This is reasonable because Ryugu's visible spectra are featureless from the b-band to x-band, including the v-band[6].

Visible spectral shape changes (for example, object size with respect to the field of view) are a known issue and depend on the spacecraft altitude[20]. Objects appear redder at low altitude and attribute the broad element of the scattering function[44], which is enhanced at lower altitudes and longer and shorter wavelengths. To correct the observation altitude difference between regions A, B, C, E and ID69, we factored those regional spectra to match with the same regional spectra observed in box A obtained on 10 July 2018 at an altitude of 20 km. The offsets in the v–x slopes range from 0.08 to 0.13 μm⁻¹ depending on the regions, and the corrected v–x slope values are shown in Fig. 4b,d and Extended Data Fig. 6.

NIRS3 spectral analysis. We use calibrated NIRS3 reflectance spectra acquired on 31 October 2018 to spectrally characterize the ID69 crater where one hotspot was detected. The observation resolution for the six extracted spectra is ~8 m per pixel, which is close to the diameter size of the crater but larger than the identified hotspot HS2. We also extracted 14 spectra acquired on the same observation day under the same conditions in the crater vicinity to compare the spectral properties between the hotspot and crater surroundings. Other NIRS3 observations with sufficiently high resolution are not available for the characterization of this small hotspot. The crater where HS1 was detected cannot be characterized in the near-infrared because it is too small and no high-resolution NIRS3 observations of this crater are available. The successive calibration steps to convert the raw data to reflectance are detailed in previous studies[22,46]. The reflectance factor is corrected to the standard viewing geometry with incidence, emergence and phase angles of 30°, 0° and 30°, respectively.

We computed an average spectrum for the hotspot using the spectra that fall on the crater (blue boxes in Fig. 2c) and an average spectrum for the hotspot vicinity using the spectra that fall just outside of the ID69 crater (orange boxes in Fig. 2c). We computed error bars on the average spectra by evaluating the standard deviation among the spectra on and off of the hotspot. Very slight differences are observed in the spectra between those that include or exclude the hotspot. To highlight the potential subtle spectral differences, we normalized the average spectra of the hotspot with the average spectra in the crater vicinity. The error bars on the normalized spectrum are calculated from the law of propagation of error:

$$\frac{(\bar{R}_{on} \pm \sigma_{on})}{(\bar{R}_{off} \pm \sigma_{off})} = \frac{\bar{R}_{on}}{\bar{R}_{off}} \pm \sqrt{\left(\frac{\sigma_{on}}{\bar{R}_{off}}\right)^2 + \left(\frac{\bar{R}_{on}}{\bar{R}_{off}^2}\sigma_{off}\right)^2}, \tag{8}$$

where $\bar{R}_{on}$ is the average spectra on the ID69 crater including the hotspot, $\bar{R}_{off}$ corresponds to the surrounding area off of the hotspot, and σ_{on} and σ_{off} are the corresponding standard deviations, respectively. The ratioed spectra are shown in Fig. 2d. We were able to highlight an increase of band depth at 2.72 μm of a few percent for the spectra on the hotspot. An increase of the absorption strength at 2.72 μm has been observed in numerous craters and might be globally attributed to similar material to the hotspot, which is too small to be resolved in the TIR images[47].

For comparison, we performed the same analysis on the ID46 crater. We used the calibrated NIRS3 spectra acquired on 30 October 2018 with a resolution of 12 m per pixel, which is smaller than the crater size. We extracted nine spectra inside the crater, where no hotspot has been detected with thermal and visible images, and 47 spectra outside of the crater that were acquired on the same day to perform a spectral comparison. We used these observations for comparison with the ID69 crater because they were acquired at similar times and with similar footprints. In Extended Data Fig. 4d, we show the spectral ratio of the average spectra inside the crater by the average spectra outside of the ID46 crater. With spectra of similar resolution for this crater, we do not observe the same trend as in the ID69 crater. Specifically, no significant increase of the absorption feature at 2.72 μm is observed.

Possible origins of the highly porous consolidated materials. There are several possibilities to explain the formation of consolidated materials with extremely high porosity of the hotspots ($\phi > 70\%$). Thermal fatigue (fracturing by thermal cycling)[27] is a potential mechanism to enhance the rock's porosity. In this case, however, since most of the boulders at least adjacent to HS1 and HS2 should have experienced a similar thermal cycling, the very limited number of the hotspots on Ryugu cannot be explained. A highly porous structure that was attributed to the removal of water ice that once filled pore space was identified in a carbonaceous chondrite Acfer 094[48]. But, its porosity is approximately 40%, less than that of hotspots. Because the SCI crater does not show any hotspot, a single cratering event, or impact, is unlikely. However, Ryugu's materials have experienced many precursor impact processes, including micrometeorite impacts, the more energetic catastrophic disruption of the parent body and impacts of S-type materials[20]. During these numerous impact processes, brecciation of the materials may occur and somewhat enhance the porosity. In fact, many boulders on Ryugu's surface showed the morphological features consistent with breccia[6] and most of the carbonaceous chondrites show brecciated structures[49]. However, it is unknown whether highly porous breccia can be formed during these energetic impacts, because we do not have natural brecciated samples, including the chondritic meteorites and lunar brecciated rocks, with such a high porosity[50–52].

Although all of these potential processes might contribute partially to the high porosity observed, the dust aggregation process through slow-velocity impacts of dusts and/or pebbles in the early solar nebula is predicted to result in such highly porous materials[2,26]. The consolidation of the dust aggregates would occur during the thermal evolution of the parent body (see below). In any case, the highly porous materials should have experienced a different history from the other abundant materials on Ryugu.

Thermal evolution of the parent body. The porous nature of the boulders on Ryugu would have originated from some partial compaction processes of an initially porous and unconsolidated planetesimal, in which highly porous materials (porosity >60%) like the hotspots, intermediately porous materials (30% < porosity < 60%) like the common boulders on Ryugu and compact materials (porosity <30%) like the cold spots formed. All of the boulders would need to be partially consolidated in the planetesimal to survive after the catastrophic disruption. The main consolidation mechanism would be hot pressing, that is, sintering and creep processes of dust grains in the planetesimals, which strongly depend on temperature and pressure. Additional cementation process would be caused by the mineral dissolution and reprecipitation onto the necks between grains. We investigated the thermal evolution of porous planetesimals by applying the methodology by Neumann et al.[29] (see also Neumann and Kruse[53] and Neumann et al.[54] for model applications to water-rich objects).

We simulated the thermal history and resulting final porosity distribution in the planetesimals to find a parent body that reproduces the porosity population measured on Ryugu (Extended Data Fig. 7c) by solving the one-dimensional heat conduction equation. A homogeneous initial porosity of 90% is assumed, whereas Neumann et al.[29] investigated the evolution of planetesimals with an initial porosity ranging from 50% to 80%. The other assumed parameters are exactly the same as

those in Neumann et al.[29] The initial composition is olivine and water ice with mass fractions of 80% and 20%, respectively. Hydration of part of the olivine is assumed after reaching 274 K (melting point of ice) as a quasi-instantaneous process that results in a serpentine fraction of 84%. The compaction of a two-component mixture of serpentine and olivine is simulated according to theoretical and experimental results of hot pressing. The porosity ϕ is calculated as:

$$\frac{\partial \log(1-\phi)}{\partial t} = \dot{\epsilon} = \nu_{se}\dot{\epsilon}_{se} + \nu_{ol}\dot{\epsilon}_{ol}, \qquad (9)$$

with bulk strain rate $\dot{\epsilon}$ and volume fraction ν_{se} and ν_{ol} and strain rates $\dot{\epsilon}_{se}$ and $\dot{\epsilon}_{ol}$ of serpentine and olivine, respectively. The strain rates are given by creep laws for minerals involved. For serpentine[55]:

$$\dot{\epsilon}_{se} = \exp(\alpha\chi)\, 4 \times 10^{-22}\sigma^2 \exp\left(-\frac{27}{RT}\left(1 - \frac{\sigma}{2.7 \times 10^9}\right)\right), \qquad (10)$$

with an effective stress σ in Pa, gas constant $R = 0.008314\,\text{kJ}\,\text{K}^{-1}\,\text{mol}^{-1}$ and temperature T. For olivine[56]:

$$\dot{\epsilon}_{ol} = \exp(\alpha\chi)\, 1.26 \times 10^{-18}\sigma^{1.5}b^{-1.4} \exp\left(-\frac{356}{RT}\right), \qquad (11)$$

with a particle grain diameter $b = 1\,\mu\text{m}$ (typical for matrix grain sizes of CI and CM chondrites[57,58]). The exponential term $\exp(\alpha\chi)$ accounts for the enhancement of the strain rate in presence of liquid water (this approach is analogous to the strain-rate enhancement in presence of silicate melt[59]). Here, $\alpha = 26$ is an empirical constant and $\chi = 0.1$ is the free water volume fraction assumed after the melting of a CM-like initial ice volume fraction of 0.2 in the initial ice–dust mixture and consumption of a half of the water for the silicate hydration. Thermal conductivity is given as an exponential function of porosity, in which the compaction by hot pressing enhances the thermal conductivity.

Extended Data Fig. 8a–d shows examples of the potential parent body with a reference radius (determined from the total mass assuming zero porosity) of $R = 2$–$5\,\text{km}$ and accretion time of $t_0 = 2.2\,\text{Myr}$ after the formation of calcium-aluminium-rich inclusions. The final porosity fraction (right panels for each result) for $R = 3\,\text{km}$ (Extended Data Fig. 8b) is most consistent with that of the boulders on Ryugu, that is, high abundance of boulders with porosities between 30% and 60% and small fraction of higher and lower porosities, corresponding to the hotspots and cold spots, respectively. Furthermore, the peak temperatures of the abundant materials ($30\% < \phi < 60\%$, left panels in Extended Data Fig. 8) range from 600 to 800 K, which is consistent with the estimated hydration temperature range (573–973 K) from the hydroxyl-band features in the SCI crater, as well as on the global scale[23], and are mostly homogeneous ($\sim$800 K), which is consistent with the globally uniform visible and infrared spectra on Ryugu[6,22]. The materials with $\phi > 60\%$, including the hotspots, would have experienced lower temperatures and were less dehydrated. Indeed, the near-infrared observation of the ID69 crater, where HS2 is located near the centre, shows a slightly stronger hydroxyl-band absorption than the surroundings by a few percent (Fig. 2d). This deeper absorption can be explained as the freshness of the ID69 crater to have avoided the solar radiative heating in the past, but this absorption feature might be partially attributed to the less-dehydrated nature of HS2 resulting from the low peak temperature in the parent body. Because the NIRS3 spot sizes ($\sim$8 m) are larger than the HS2 size ($\sim$3 m), the observed spectra are a mixture of those of the hotspot and its surroundings. The strong hydroxyl-band absorption would therefore be somewhat weakened for the hotspot.

On the other hand, numerical and observational studies on planetary growth suggest the formation of larger planetesimals of typically 100 km size[1,60,61]. The larger bodies (for example, 20–100 km) might also allow porous materials to form in the near-surface layer as the origin of Ryugu's boulders. However, those bodies would be dominated by low-porosity material with $\phi < 60\%$ (Extended Data Figs. 8e–j) and produce a very small fraction of higher-porosity consolidated materials. Because of the depleted radioactive heat source, bodies that accreted at a later time, for example, $t_0 \geq 3$ Myr, had overall peak temperatures of ≤ 500 K ($R = 20$ km) and ≤ 600 K ($R = 100$ km), which are lower than the hydration temperature of the Ryugu material[23]. Large parent bodies would be therefore unlikely to produce the boulder porosity distribution found on Ryugu. It should be noted that the preferred parent body with $R = 3$ km and $t_0 = 2.2$ Myr would not be a unique solution to produce Ryugu's boulder porosity distribution because the calculation results strongly depend on the many parameters, including initial porosity (here 90%) and composition.

Data availability
All images and essential data used in this study are available at the JAXA Data Archives and Transmission System (DARTS) at http://www.darts.isas.jaxa.jp/pub/hayabusa2/paper/Sakatani_2021. The other data that support the plots within this paper are available from the corresponding author upon reasonable request.

References
1. Okuzumi, S., Tanaka, H., Kobayashi, H. & Wada, K. Rapid coagulation of porous dust aggregates outside the snow line: a pathway to successful icy planetesimal formation. *Astrophys. J.* **752**, 106 (2012).
2. Kataoka, A., Tanaka, H., Okuzumi, S. & Wada, K. Fluffy dust forms icy planetesimals by static compression. *Astron. Astrophys.* **557**, L4 (2013).
3. Neumann, W., Breuer, D. & Spohn, T. Modelling of compaction in planetesimals. *Astron. Astrophys.* **567**, A120 (2014).
4. Grott, M. et al. Low thermal conductivity boulder with high porosity identified on C-type asteroid (162173) Ryugu. *Nat. Astron.* **3**, 971–976 (2019).
5. Okada, T. et al. Highly porous nature of a primitive asteroid revealed by thermal imaging. *Nature* **579**, 518–522 (2020).
6. Sugita, S. et al. The geomorphology, color, and thermal properties of Ryugu: implications for parent-body processes. *Science* **364**, eaaw0422 (2019).
7. Groussin, O. et al. The thermal, mechanical, structural, and dielectric properties of cometary nuclei after Rosetta. *Space Sci. Rev.* **215**, 29 (2019).
8. Weissman, P., Morbidelli, A., Davidsson, B. & Blum, J. Origin and evolution of cometary nuclei. *Space Sci. Rev.* **216**, 6 (2020).
9. Arakawa, M. et al. An artificial impact on the asteroid (162173) Ryugu formed a crater in the gravity-dominated regime. *Science* **368**, 67–71 (2020).
10. Tsuda, Y. et al. Hayabusa2 mission status: landing, roving and cratering on asteroid Ryugu. *Acta Astronaut.* **171**, 42–54 (2020).
11. Morota, T. et al. Sample collection from asteroid (162173) Ryugu by Hayabusa2: implications for surface evolution. *Science* **368**, 654–659 (2020).
12. Cho, Y. et al. Geologic history and crater morphology of asteroid (162173) Ryugu. Preprint at https://doi.org/10.1002/essoar.10506689.2 (2021).
13. Shimaki, Y. et al. Thermophysical properties of the surface of asteroid 162173 Ryugu: infrared observations and thermal inertia mapping. *Icarus* **348**, 113835 (2020).
14. Sakatani, N. et al. Thermal conductivity model for powdered materials under vacuum based on experimental studies. *AIP Adv.* **7**, 015310 (2017).
15. Biele, J. et al. Effects of dust layers on thermal emission from airless bodies. *Prog. Earth Planet. Sci.* **6**, 48 (2019).
16. Jaumann, R. et al. Images from the surface of asteroid Ryugu show rocks similar to carbonaceous chondrite meteorites. *Science* **365**, 817–820 (2019).
17. Noguchi, R. et al. Crater depth-to-diameter ratios on asteroid 162173 Ryugu. *Icarus* **354**, 114016 (2021).
18. Roberts, J. H. et al. Origin and flatness of ponds on asteroid 433 Eros. *Meteorit. Planet. Sci.* **49**, 1735–1748 (2014).
19. Rozitis, B. et al. Asteroid (101955) Bennu's weak boulders and thermally anomalous equator. *Sci. Adv.* **6**, eabc3699 (2020).
20. Tatsumi, E. et al. Collisional history of Ryugu's parent body from bright surface boulders. *Nat. Astron.* **5**, 39–45 (2020).
21. Ryan, A. J., Pino Muñoz, D., Bernacki, M. & Delbo, M. Full-field modeling of heat transfer in asteroid regolith: radiative thermal conductivity of polydisperse particulates. *J. Geophys. Res. Planets* **125**, e2019JE006100 (2020).
22. Kitazato, K. et al. The surface composition of asteroid 162173 Ryugu from Hayabusa2 near-infrared spectroscopy. *Science* **364**, 272–275 (2019).
23. Kitazato, K. et al. Thermally altered subsurface materials of asteroid 162173 Ryugu. *Nat. Astron.* **5**, 246–250 (2021).
24. Potin, S., Beck, P., Schmitt, B. & Moynier, F. Some things special about NEAs: geometric and environmental effects on the optical signatures of hydration. *Icarus* **333**, 415–428 (2019).
25. Carry, B. Density of asteroids. *Planet. Space Sci.* **73**, 98–118 (2012).
26. Blum, J. Dust evolution in protoplanetary discs and the formation of planetesimals: What have we learned from laboratory experiments? *Space Sci. Rev.* **214**, 52 (2018).
27. Delbo, M. et al. Thermal fatigue as the origin of regolith on small asteroids. *Nature* **508**, 233–236 (2014).
28. Hartzell, C. M. & Scheeres, D. J. Dynamics of levitating dust particles near asteroids and the Moon. *J. Geophys. Res. Planets* **118**, 116–125 (2013).
29. Neumann, W. et al. Microporosity and parent body of the rubble-pile NEA (162173) Ryugu. *Icarus* **358**, 114166 (2021).
30. Takita, J., Senshu, H. & Tanaka, S. Feasibility and accuracy of thermophysical estimation of asteroid 162173 Ryugu (1999 JU3) from the Hayabusa2 thermal infrared imager. *Space Sci. Rev.* **208**, 287–315 (2017).
31. Ishiguro, M. et al. Optical properties of (162173) 1999 JU3: in preparation for the JAXA Hayabusa 2 sample return mission. *Astrophys. J.* **792**, 74 (2014).
32. Vasavada, A. R. et al. Lunar equatorial surface temperatures and regolith properties from the diviner lunar radiometer experiment. *J. Geophys. Res. E* **117**, E00H18 (2012).
33. Miura, A., Sakatani, N., Yokota, Y. & Honda, R. A study on methods of generating asteroid shape models. *J. Space Sci. Inform. Jpn* **9**, 33–44 (2020).
34. Matsumoto, K. et al. Improving Hayabusa2 trajectory by combining LIDAR data and a shape model. *Icarus* **338**, 113574 (2020).
35. Senshu, H. et al. Numerical simulation on the thermal moment from Ryugu-like rough surface asteroid. In *Proc. 51st Lunar and Planetary Science Conference* abstr. 1990 (Lunar and Planetary Institute, 2020).

36. Hamm, M. et al. Thermal conductivity and porosity of Ryugu's boulders from in-situ measurements of MARA—the MASCOT radiometer. In *Proc. 50th Lunar and Planetary Science Conference* abstr. 1373 (Lunar and Planetary Institute, 2019).

37. Avdellidou, C. et al. Very weak carbonaceous asteroid simulants I: mechanical properties and response to hypervelocity impacts. *Icarus* **341**, 113648 (2020).

38. Grott, M. et al. Macroporosity and grain density of rubble pile asteroid (162173) Ryugu. *J. Geophys. Res. Planets* **125**, e2020JE006519 (2020).

39. Flynn, G. J., Consolmagno, G. J., Brown, P. & Macke, R. J. Physical properties of the stone meteorites: implications for the properties of their parent bodies. *Chem. Erde* **78**, 269–298 (2018).

40. Wada, K. et al. Asteroid Ryugu before the Hayabusa2 encounter. *Prog. Earth Planet. Sci.* **5**, 82 (2018).

41. Krause, M., Blum, J., Skorov, Y. V. & Trieloff, M. Thermal conductivity measurements of porous dust aggregates: I. Technique, model and first results. *Icarus* **214**, 286–296 (2011).

42. Krause, M. et al. Modeling the early thermal evolution of meteorite parent bodies based on new thermal conductivity measurements of highly porous aggregates. In *Proc. 42nd Lunar and Planetary Science Conference* abstr. 2696 (Lunar and Planetary Institute, 2011).

43. Blum, J. & Schräpler, R. Structure and mechanical properties of high-porosity macroscopic agglomerates formed by random ballistic deposition. *Phys. Rev. Lett.* **93**, 115503 (2004).

44. Tatsumi, E. et al. Updated inflight calibration of Hayabusa2's optical navigation camera (ONC) for scientific observations during the cruise phase. *Icarus* **325**, 153–195 (2019).

45. Tatsumi, E. et al. Global photometric properties of (162173) Ryugu. *Astron. Astrophys.* **639**, A83 (2020).

46. Iwata, T. et al. NIRS3: the near infrared spectrometer on Hayabusa2. *Space Sci. Rev.* **208**, 317–337 (2017).

47. Riu, L. et al. Spectral characterization of the craters of Ryugu as observed by the NIRS3 instrument on-board Hayabusa2. *Icarus* **357**, 114253 (2021).

48. Matsumoto, M. et al. Discovery of fossil asteroidal ice in primitive meteorite Acfer 094. *Sci. Adv.* **5**, eaax5078 (2019).

49. Bischoff, A., Scott, E. R. D., Metzler, K. & Goodrich, C. A. in *Meteorites and the Early Solar System II* (eds Lauretta, D. & McSween, H. Y.) 679–712 (Univ. Arizona Press, 2006).

50. Consolmagno, G. J., Britt, D. T. & Macke, R. J. The significance of meteorite density and porosity. *Chem. Erde* **68**, 1–29 (2008).

51. Macke, R. J., Consolmagno, G. J. & Britt, D. T. Density, porosity, and magnetic susceptibility of carbonaceous chondrites. *Meteorit. Planet. Sci.* **46**, 1842–1862 (2011).

52. Kiefer, W. S., Macke, R. J., Britt, D. T., Irving, A. J. & Consolmagno, G. J. The density and porosity of lunar rocks. *Geophys. Res. Lett.* **39**, L07201 (2012).

53. Neumann, W. & Kruse, A. Differentiation of Enceladus and retention of a porous core. *Astrophys. J.* **882**, 47 (2019).

54. Neumann, W., Jaumann, R., Castillo-Rogez, J., Raymond, C. A. & Russell, C. T. Ceres' partial differentiation: undifferentiated crust mixing with a water-rich mantle. *Astron. Astrophys.* **633**, A117 (2020).

55. Amiguet, E. et al. Creep of phyllosilicates at the onset of plate tectonics. *Earth Planet. Sci. Lett.* **345–348**, 142–150 (2012).

56. Schwenn, M. B. & Goetze, C. Creep of olivine during hot-pressing. *Tectonophysics* **48**, 41–60 (1978).

57. Cloutis, E. A., Hiroi, T., Gaffey, M. J., Alexander, C. M. O. D. & Mann, P. Spectral reflectance properties of carbonaceous chondrites: 1. CI chondrites. *Icarus* **212**, 180–209 (2011).

58. Cloutis, E. A., Hudon, P., Hiroi, T., Gaffey, M. J. & Mann, P. Spectral reflectance properties of carbonaceous chondrites: 2. CM chondrites. *Icarus* **216**, 309–346 (2011).

59. Mei, S., Bai, W., Hiraga, T. & Kohlstedt, D. L. Influence of melt on the creep behavior of olivine–basalt aggregates under hydrous conditions. *Earth Planet. Sci. Lett.* **201**, 491–507 (2002).

60. Klahr, H. & Schreiber, A. Turbulence sets the length scale for planetesimal formation: local 2D simulations of streaming instability and planetesimal formation. *Astrophys. J.* **901**, 54 (2020).

61. Klahr, H. & Schreiber, A. Testing the Jeans, Toomre, and Bonnor-Ebert concepts for planetesimal formation: 3D streaming instability simulations of diffusion-regulated formation of planetesimals. *Astrophys. J.* **911**, 9 (2021).

62. Opeil, C. P., Consolmagno, G. J., Safarik, D. J. & Britt, D. T. Stony meteorite thermal properties and their relationship with meteorite chemical and physical states. *Meteorit. Planet. Sci.* **47**, 319–329 (2012).

63. Hamm, M., Pelivan, I., Grott, M. & de Wiljes, J. Thermophysical modelling and parameter estimation of small Solar System bodies via data assimilation. *Mon. Not. R. Astron. Soc.* **496**, 2776–2785 (2020).

Author contributions

N.S. led this study and analysis TIR and ONC-T data. TIR development, data acquisitions, reductions: N.S., S. Tanaka, T.O., T.F. T. Kouyama, H. Senshu., Y.S., T.A., J.T., H.D., T. Sekiguchi, M.T., Y.O., T. Matsunaga, T.W., S. Hasegawa, J.H. and A.M. Thermal modelling of Ryugu's surfaces and TIR data analysis: N.S., S. Tanaka, H. Senshu, J.T., T.G.M., A. Hagermann, J.B., M.G., M. Hamm and M.D. ONC-T development, data acquisitions, reductions and analysis: N.S., S. Sugita, R.H., T. Morota, S. Kameda, Y. Yokota, E.T., K. Yumoto, M. Yamada, H. Suzuki, C. Honda, K.O., M. Hayakawa, K. Yoshioka, M.M., Y.C. and H. Sawada. NIRS3 development, data acquisitions, reductions and analysis: L.R., K.K., T.I., M. Abe, M. Ohtake and S.M. Shape model construction and evaluation: N. Hirata (Univ. Aizu), N. Hirata (Kobe Univ.), S. Sugita, R.N., Y.S., S.W. and A.M. Thermal evolution modelling of the parent body: W.N., N.S. and M.G. LIDAR-derived trajectory: K.M., H.N., Y. Ishihara, K. Yamamoto, A. Higuchi, N.N. and G.O. SCI development and operations: T. Saiki, H. Imamura, Y. Takagi, H. Yano, K.S., C.O., S.N., Y. Iijima, M. Arawaka, K.W., T. Kadono, K.I. Operations of spacecraft: S. Tanaka, T.O., H. Sawada, T.I., M. Abe, G.O., T. Saiki, H. Yano, S.N., F.T., S. Kikuchi, T.Y., N.O., Y.M., K. Yoshikawa, T.T., Y. Takei, A.F., H.T., Y. Yamamoto, C. Hirose, S. Hosoda, O.M., T. Shimada, S. Soldini, R.T., M. Ozaki, M. Yoshikawa and Y. Tsuda. Project administration: S. Tanaka, T.O., S. Sugita, K.K., N.N., M. Arakawa, S. Tachibana, H. Ikeda, M.I., H. Yabuta, F.T., T. Saiki, S.N., M. Yoshikawa, S.W. and Y. Tsuda. All authors discussed the results and commented on the manuscript.

Competing interests

The authors declare no competing interests.

Additional information

Extended data is available for this paper at https://doi.org/10.1038/s41550-021-01371-7.

Supplementary information The online version contains supplementary material available at https://doi.org/10.1038/s41550-021-01371-7.

Correspondence and requests for materials should be addressed to N.S.

Peer review information *Nature Astronomy* Ben Rozitis, Andrew Ryan and Mario Trieloff for their contribution to the peer review of this work.

Reprints and permissions information is available at www.nature.com/reprints.

Publisher's note Springer Nature remains neutral with regard to jurisdictional claims in published maps and institutional affiliations.
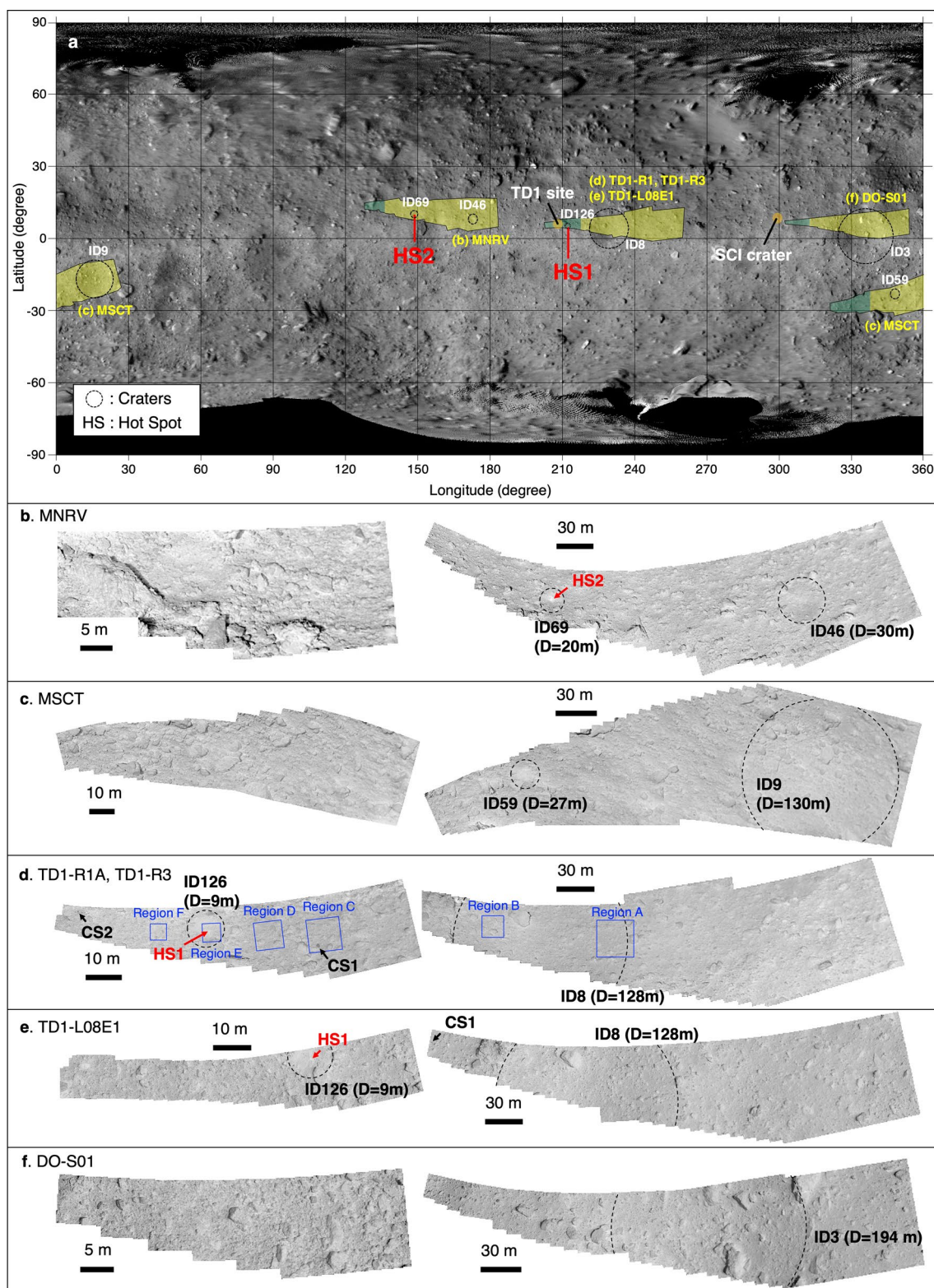
Extended Data Fig. 1 | Field of view by high-resolution TIR data and mosaic images by TIR during the descent operations. a, Global map of Ryugu by ONC-T[6] and coverage of the TIR images during the descent sequences used in this paper (see also Supplementary Table 1). Abbreviations of the sequences are, MNRV: MINERVA-II rovers separation, MSCT: MASCOT lander separation, TD1-R1A and TD1-R3: Touch-down rehearsals, TD1-L08E1: First touch-down operation, and DO-S01: Descent operation for S01 region. The TIR coverage is about 5% of the total Ryugu surface area. Dashed circles denote the craters (IDs 3, 8, 9, 46, 59, 69, and 126) in the TIR footprints. First touch-down (TD1) site and SCI crater site are also shown in this map. **b-f,** Mosaics of TIR images acquired during the descent operations (images in hovering and ascending phases are not included). The right and left panels show images at higher and lower altitudes, whose footprints on the global map are roughly indicated as yellow and green regions in **a**, respectively. The values of D adjacent to the crater IDs represent the diameters of the crater[17]. The hotspots HS1 and HS2 are indicated as red arrows. The cold spot boulders detected by Okada et al.[5] are shown as CS1 and CS2. Blue squares in **d** indicate the regions A to F shown in Fig. 3.
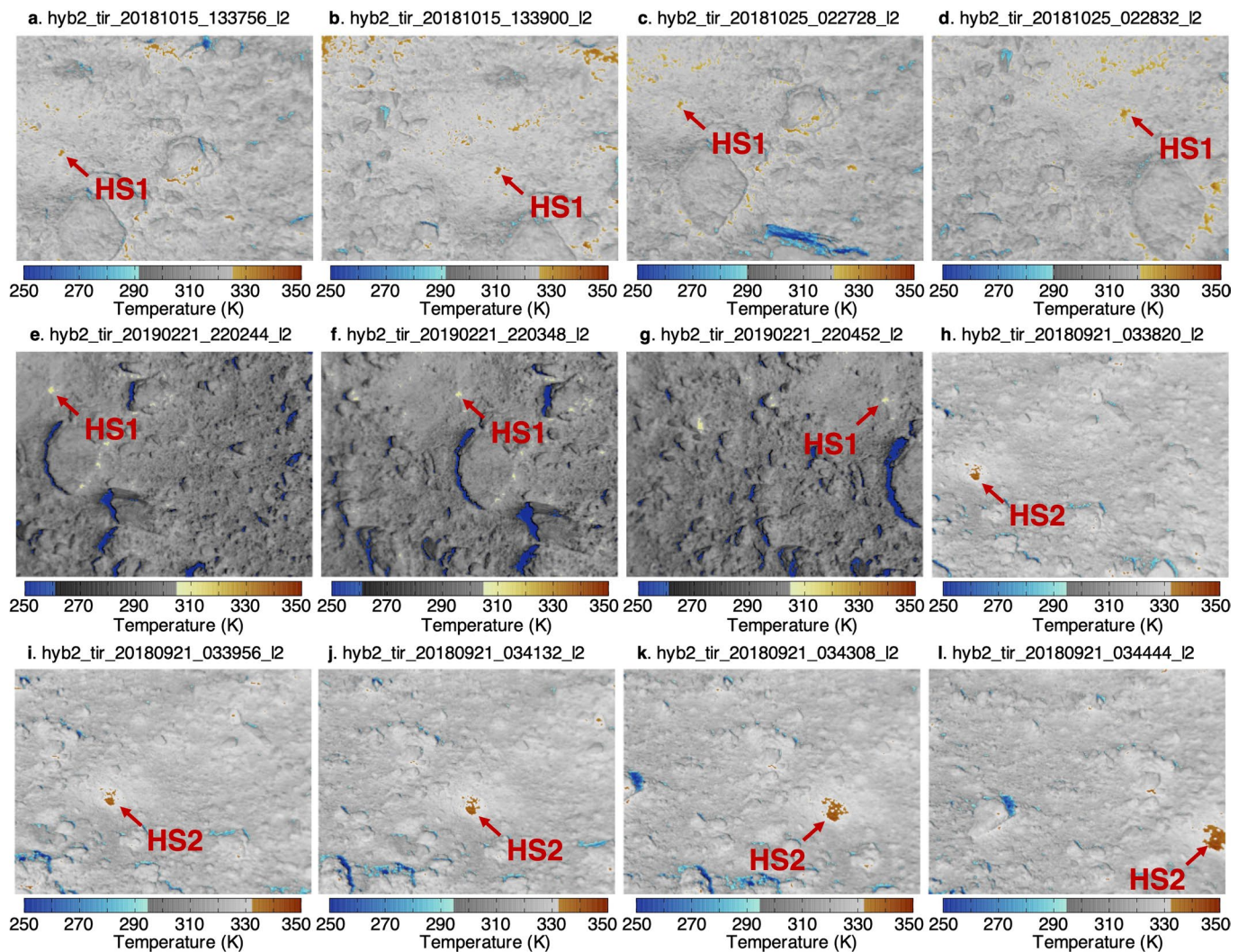
Extended Data Fig. 2 | All TIR images of hotspots HS1 and HS2. a-b, HS1 in TD1-R1A sequence. **c-d**, HS1 in TD1-R3 sequence. **e-g**, HS1 in TD1-L08E1 sequence. **h-l**, HS2 in MNRV sequence. File names are indicated as labels. Coloured pixels indicate regions that are hotter or colder by more than 2σ of the mean temperature relevant to each operation (Supplementary Table 1). Gray-scaled pixels are within 2σ of the averages. The temperatures of HS1 and HS2 are consistently higher than the surroundings although the observation geometries (for example, solar incident angle, emission angle) differ, which suggests lower TI regardless of microscopic roughness.
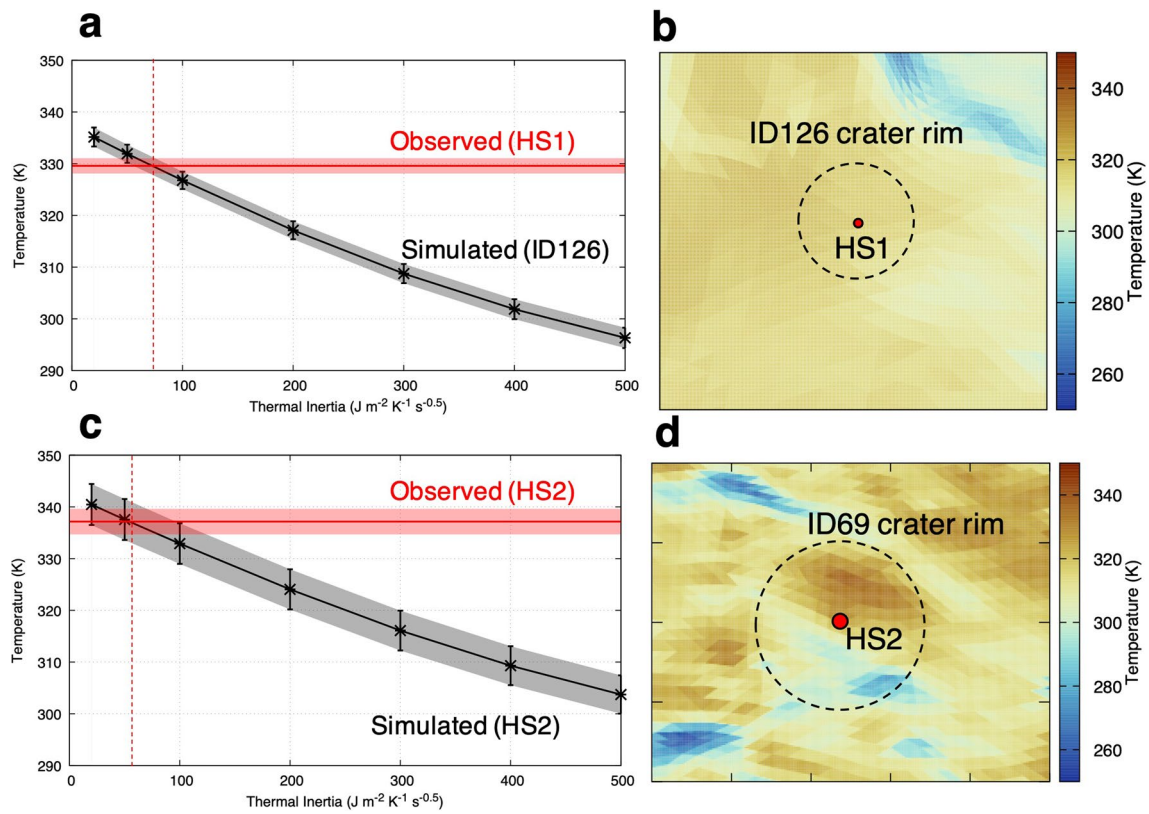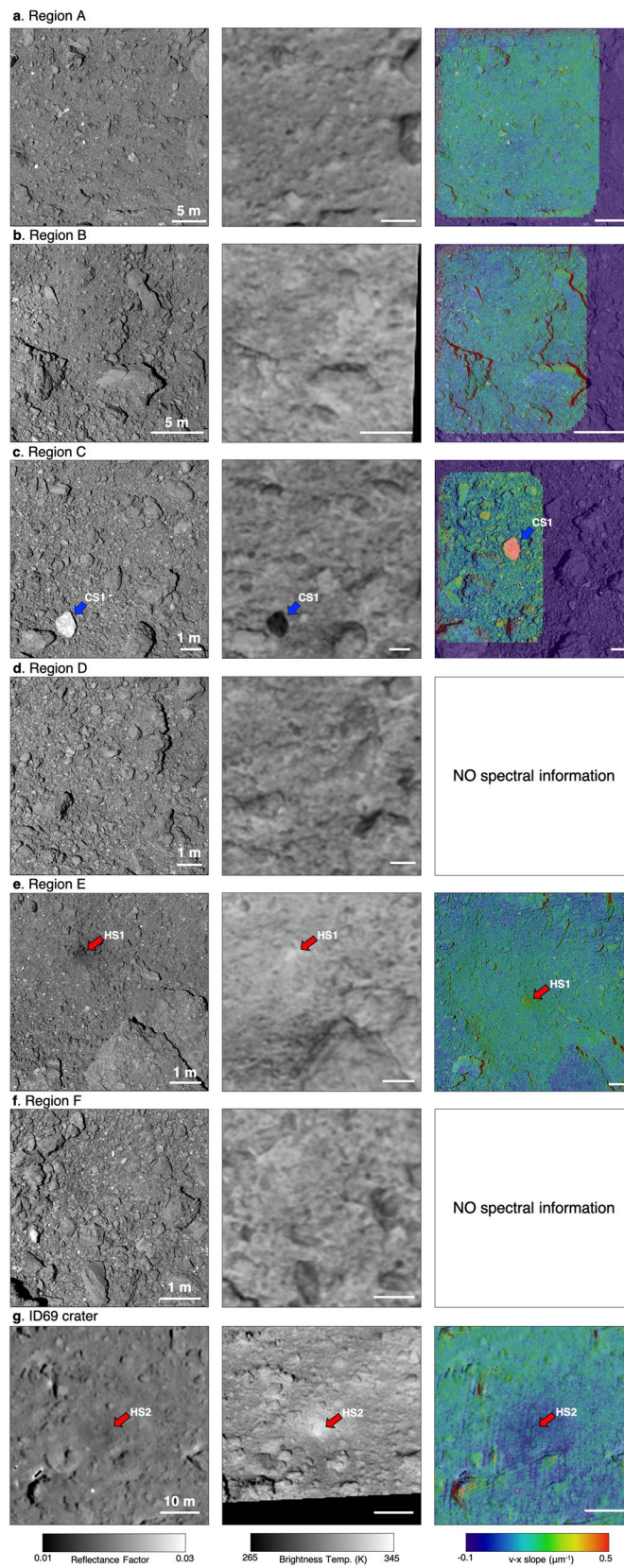
Extended Data Fig. 3 | Estimation of the thermal inertia of hotspots. a, Comparison of simulated temperature averaged in the ID126 crater with variable thermal inertia (black line) and observed temperature for the hotspot (red horizontal line). The error bars show the standard deviation within the relevant pixels. By comparing the observed HS1 temperature with the simulated average temperatures in the ID126 crater, the best-fit TI value is 73 tiu for the hotspot. **b**, Simulated temperature image around ID126 crater (dashed circle) with TI = 200 tiu. The position of HS1 is indicated as red point. **c**, Similar to **a** but for hotspot HS2. The simulated data are the average of the hotspot (red-filled circle) in the simulated image of **d**.
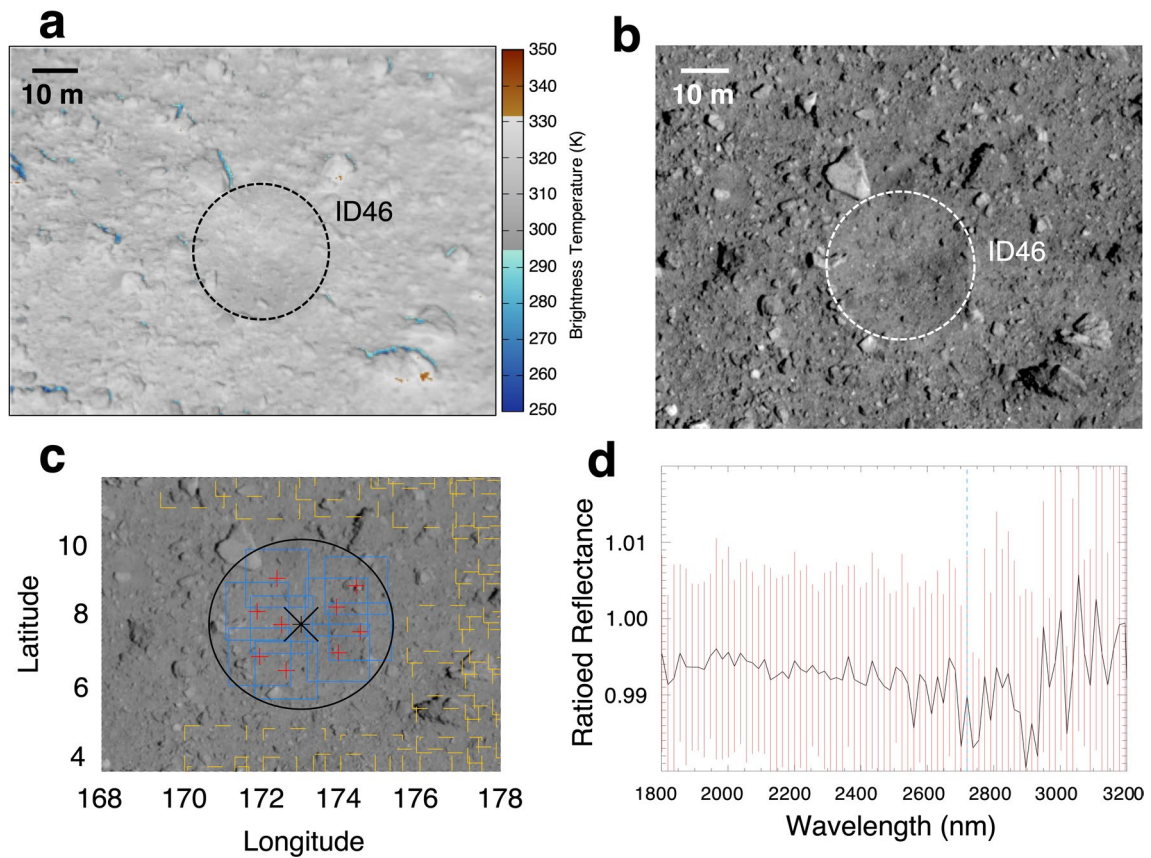
Extended Data Fig. 4 | TIR and NIRS3 data for ID46 crater without the hotspot. TIR (**a**) and ONC-T (**b**) images for the ID46 crater (7.8°N, 173.0°E) without hotspots (hyb2_tir_20180921_031212_l2 and hyb2_onc_20190307_222828_tvf_l2b, respectively). The crater rim is denoted as dashed circles. Only the hot or cold regions are coloured in the TIR image (see also Extended Data Fig. 2). **c**, NIRS3 footprint on 30 October 2018. Blue rectangles denote the NIRS3 footprints inside the crater, and yellow rectangles denote those of the outside. **d**, reflectance ratio of centre-to-rim of the crater. In contrast with the ID69 crater (Fig. 2d), an absorption increase at 2.72 μm does not appear in the ID46 crater.
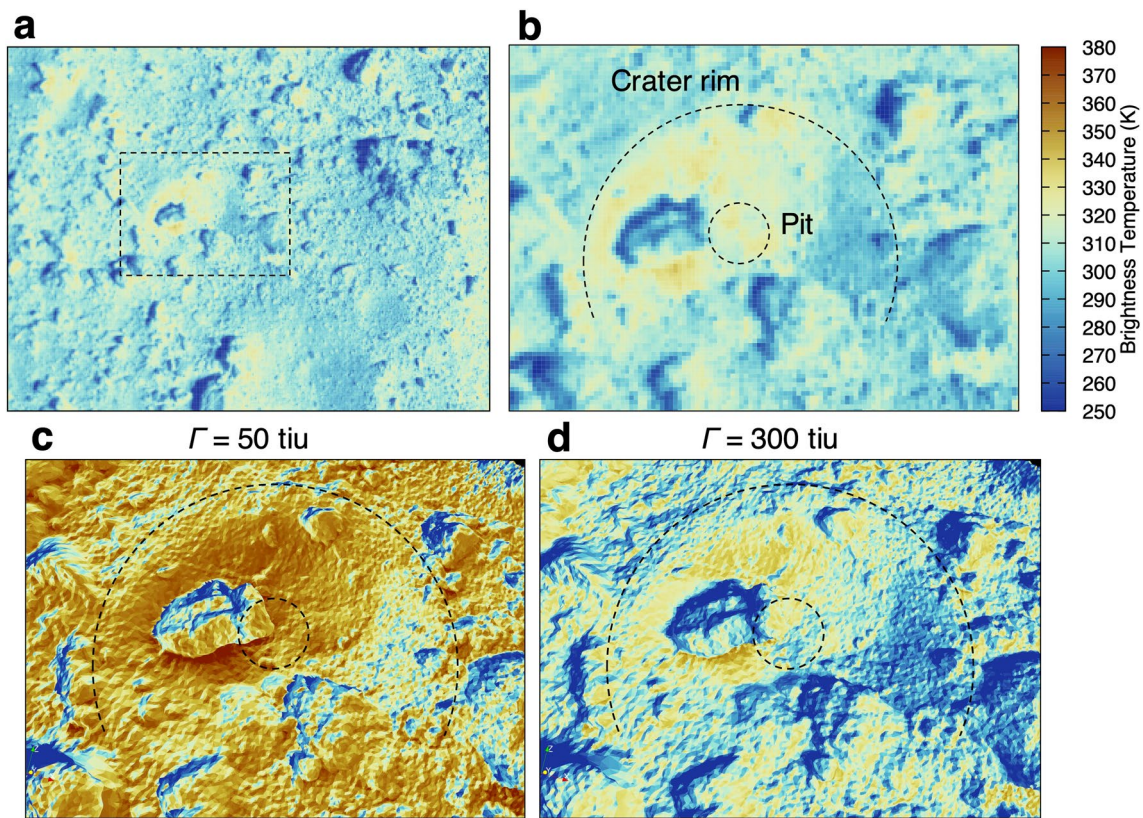
Extended Data Fig. 5 | TIR observation of SCI crater. a, TIR image of acquired during ascending phase of the PPTD-TM1B sequence. **b**, Close-up of the dashed rectangle in **a**, showing the artificial impact crater (SCI crater) at (7.9°N, 301.3°E). The rim and pit (impact points) positions are shown. Thermal calculation results using a local digital elevation model[9] with uniform thermal inertia of 50 tiu (**c**) and 300 tiu (**d**) are shown for comparison. Agreement with the observed image in **b** implies that the thermal inertia in the SCI crater is roughly 300 tiu including the central pit and/or impact site.

a. Region A

b. Region B

c. Region C

CS1

CS1

CS1

d. Region D

NO spectral information

e. Region E

HS1

HS1

HS1

f. Region F

NO spectral information

g. ID69 crater

HS2

HS2

HS2

0.01 — Reflectance Factor — 0.03

265 — Brightness Temp. (K) — 345

-0.1 — v-x slope (μm⁻¹) — 0.5

Extended Data Fig. 6 | See next page for caption.

Extended Data Fig. 6 | Visible, thermal, and spectral slope images acquired during the descent operations. a-f, ONC-T v-band reflectance factor (left), TIR brightness temperature (middle) and v-to-x slope (right) image sets in the TD1-R3 descent sequence. Superimposed images of the reflectance and temperature images are also shown in Fig. 3. **g**, Image set for the ID69 crater. TIR images are aligned on the ONC-T images by affine transformation. The v-to-x slope image of region C was created from multi-band images acquired during the TD1-L08-E1 operation and that of region E was during the TD1-R3 ascent sequence. Blue arrows in **c** indicate the bright and cold spot. Red arrows in **e** and **g** indicate the hotspots HS1 and HS2, respectively.
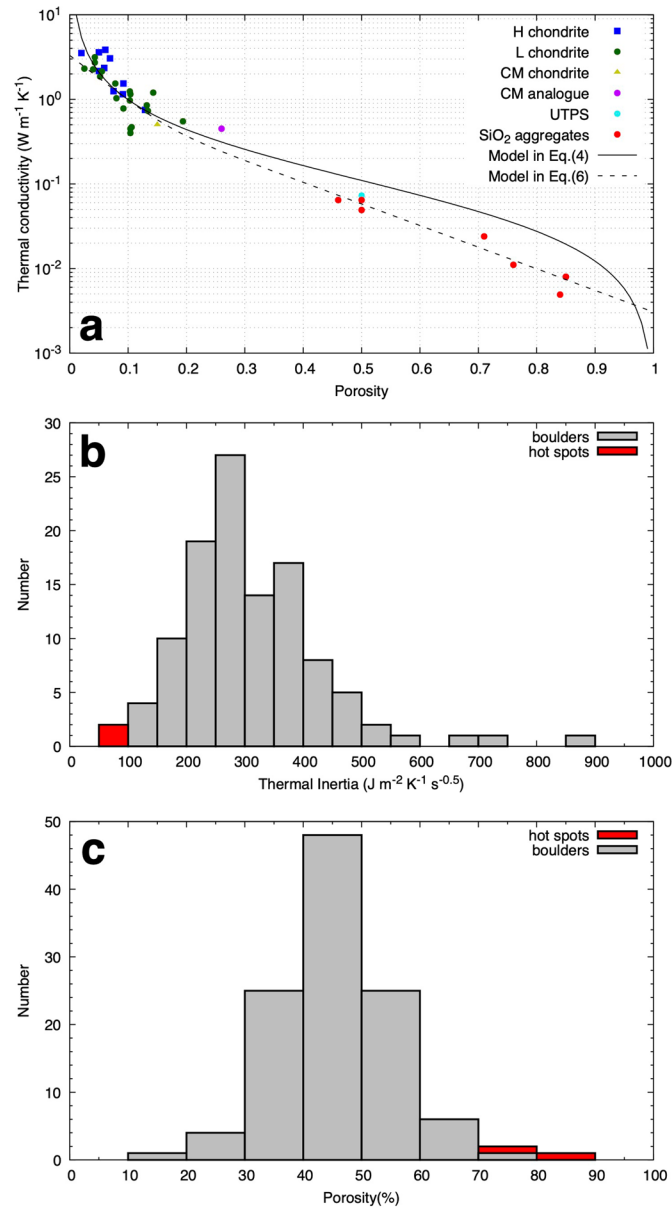
Extended Data Fig. 7 | Porosity estimate and TI and porosity distribution of boulders. a, Models of porosity dependence of thermal conductivity. The experimental data for chondritic meteorites[62], CM analogue[37], Phobos simulant UTPS[36] and SiO_2 aggregates[41] are also shown. The experimental data of the SiO_2 aggregates are multiplied by 4.3/1.4 to convert the bulk thermal conductivity (at zero porosity) of SiO_2 (1.4 W m^{-1} K^{-1}) to that of the chondritic meteorites (4.3 W m^{-1} K^{-1}). The solid and dashed curves represent Eqs. (4) and (6) in Method, respectively. **b**, Histogram of the thermal inertia for the boulders on Ryugu. Approximately 70% of the boulders have a TI ranging from 200 to 400 tiu, which is consistent with the global observations[5,13] and local observations by the MARA instrument onboard the MASCOT lander[4,63]. **c**, Histogram of the porosity ϕ of boulders on Ryugu estimated from the thermal inertia shown in Fig. 4c and the model by Krause et al.[42] (dashed curve in **a**). Approximately 90% of the boulders have a porosity between 30% and 60%.
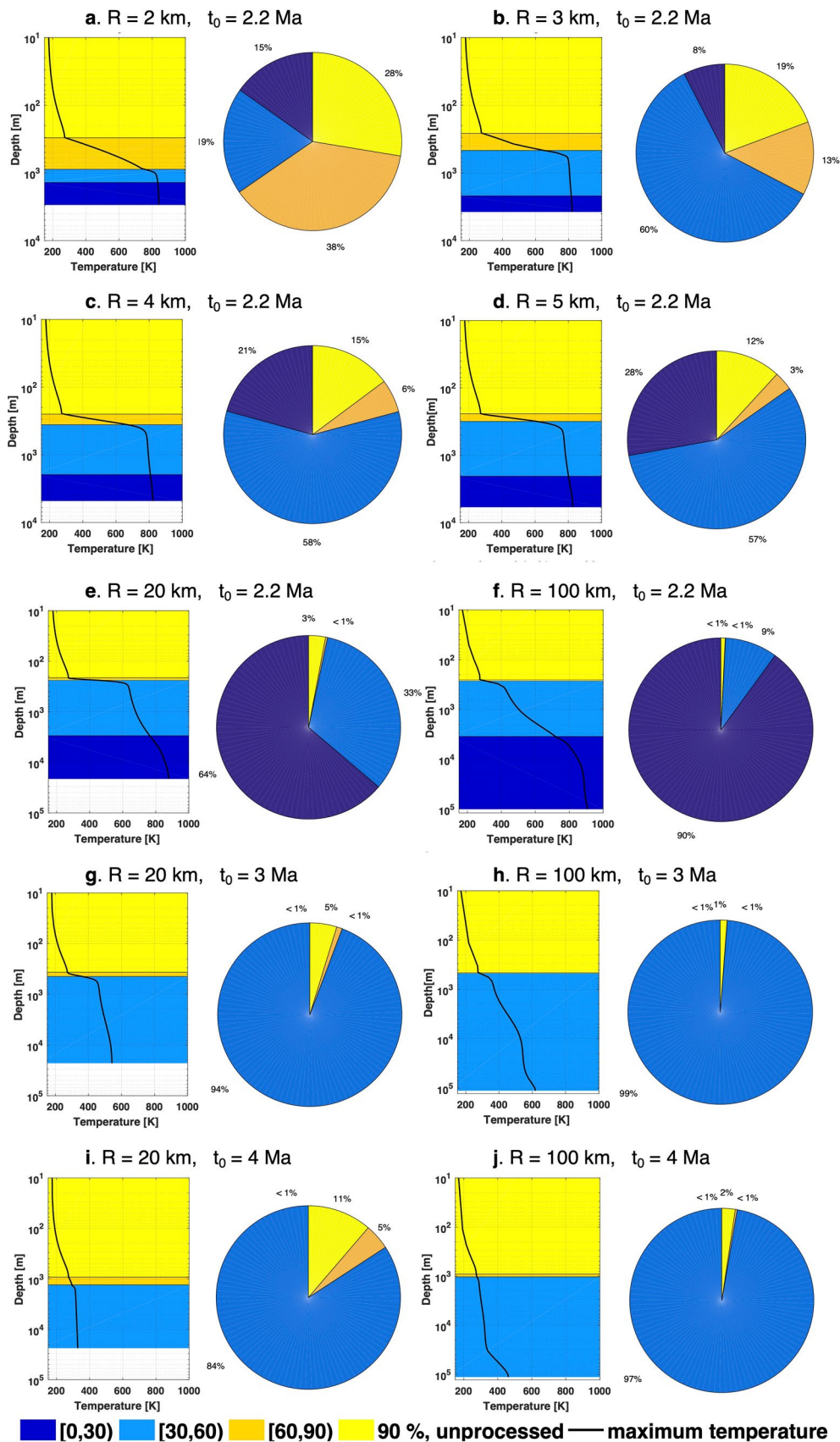
Extended Data Fig. 8 | Results of the thermal evolution modelling for parent bodies of Ryugu. a-j, Radius is given by *R* and accretion time is t_0 after CAI (calcium-aluminum-rich inclusions) formation. Left and right panels in each case show peak temperatures as a function of depth from the surface and volume fraction of the materials with different porosity ranges in the parent bodies (dark blue: $\phi < 30\%$, light blue: $30\% < \phi < 60\%$, orange: $60\% < \phi < 90\%$, and yellow: $\phi = 90\%$ unconsolidated without hot pressing), respectively.